Theoretical and Experimental Exploration of a Novel In-Plane Chemically Ordered (Cr2/3M1/3)(2)AIC i-MAX Phase with M = Scand Y

Jun Lu, Andreas Thore, Rahele Meshkian, Quanzheng Tao, Lars Hultman and Johanna Rosén

Lu, J., Thore, A., Meshkian, R., Tao, Q., Hultman, L., Rosén, J., (2017), Theoretical and Experimental Exploration of a Novel In-Plane Chemically Ordered (Cr2/3M1/3)(2)AIC i-MAX Phase with M = Sc and Y, *Crystal Growth & Design*, 17(11), 5704-5711. https://doi.org/10.1021/acs.cgd.7b00642

Original publication available at:
https://doi.org/10.1021/acs.cgd.7b00642

Cover Page

Theoretical and experimental exploration of a novel in-plane chemically-ordered $(Cr_{2/3}M_{1/3})_2AlC$ *i-MAX* phase with M=Sc and Y

Lu J*, Thore A, Meshkian R, Tao Q, Hultman L and Rosen J

Thin Film Physics, Department of Physics, Chemistry and Biology (IFM), Linköping University, SE-581 83 Linköping, Sweden

* junlu@ifm.liu.se

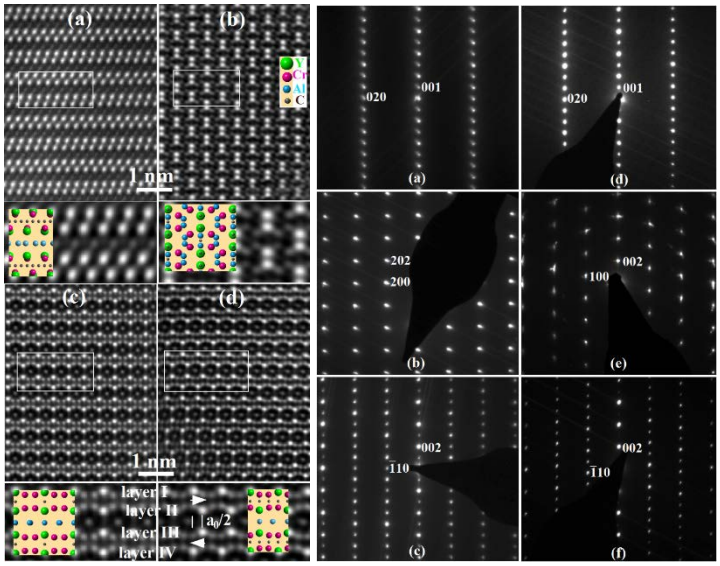

Abstract: We have uncovered two inherently laminated transition metal carbides, $(Cr_{2/3}Sc_{1/3})_2AlC$ and $(Cr_{2/3}Y_{1/3})_2AlC$, which display in-plane chemical order in the carbide sheets and a Kagomé pattern in the Al layers. The phases belong to the most recently discovered family of so called *i*-MAX phases. The materials were synthesized and the crystal structures evaluated by means of analytical high-resolution scanning transmission electron microscopy, selected area electron diffraction, and X-ray diffraction Rietveld refinement. An orthorhombic structure of space group Cmcm (#63) and a monoclinic structure of space group C2/c (#15) are identified. The compounds were investigated by first principles calculations based on density functional theory, suggesting close to degenerate antiferro- and ferromagnetic spin states, dynamical and mechanical stability, and a Voigt bulk modulus in the range 134-152 GPa.

Theoretical and experimental exploration of a novel in-plane chemically-ordered $(Cr_{2/3}M_{1/3})_2AlC$ *i-MAX* phase with M=Sc and Y

Lu J*, Thore A, Meshkian R, Tao Q, Hultman L and Rosen J

Thin Film Physics, Department of Physics, Chemistry and Biology (IFM), Linköping University, SE-581 83 Linköping, Sweden

* junlu@ifm.liu.se

Theoretical and experimental exploration of a novel in-plane chemically-ordered $(Cr_{2/3}M_{1/3})_2AlC$ *i-MAX* phase with M=Sc and Y

Lu J*, Thore A, Meshkian R, Tao Q, Hultman L and Rosen J

Thin Film Physics, Department of Physics, Chemistry and Biology (IFM), Linköping University, SE-581 83 Linköping, Sweden

* junlu@ifm.liu.se

Abstract: We have uncovered two inherently laminated transition metal carbides, $(Cr_{2/3}Sc_{1/3})_2AlC$ and $(Cr_{2/3}Y_{1/3})_2AlC$, which display in-plane chemical order in the carbide sheet and Kagomé pattern in the Al layer. The phases belong to the most recently discovered family of so called *i*-MAX phases. The materials were synthesized and the crystal structures evaluated by means of analytical high resolution scanning transmission electron microscopy, selected area electron diffraction, and X-ray diffraction Rietveld refinement. An orthorhombic structure of space group Cmcm (#63) and a monoclinic structure of space group C2/c (#15) are solved. The compounds were investigated by first principles calculations based on density functional theory, suggesting close to degenerate antiferro- and ferromagnetic spin states, dynamical and mechanical stability, and a Voigt bulk modulus in the range 134-152 GPa.

1. INTRODUCTION

Laminated materials possess unique properties rendering them suitable for, e.g., memory devices, energy storage, microelectronics, and sensors[1,2]. MAX phases, a family of hexagonal ternary carbides or nitrides including more than 70 different compounds,[3,4] are inherently laminated, displaying a unique combination of metallic and ceramic properties as well as reversible deformation[5] and bulk ripplocations.[6] The general formula of MAX phases can be expressed as $M_{n+1}AX_n$ (n=1-3), where M is a transition metal Ti, V, Cr, Mn, Mo, Hf, Sc, etc., A is group 13 to 16 element, e.g., Al, Si, Sn, Ga, Ge, and X is C or N.

In addition to traditional ternary compounds, MAX phases can form quaternary phases by alloying on the M, A or X site. This typically gives rise to solid solutions, though in 2014 Liu et al. reported an out-of-plane chemically ordered MAX phase (here denoted *o*-MAX) Cr_2TiAlC_2,[7] composed of a sandwich structure of alternating atomic layers. Similarly, *o*-MAX phases were found in the $(V,Cr)_3AlC_2$ system, the $(Mo,Ti)_{n+1}AlC_n$ (n=2-3) system,[8,9,10] and recently in the form of Mo_2ScAlC_2.[11] Hence, to date the o-MAX phases are formed only in 312 and 413 structures, and not in the 211 structure, possibly due to a high configurational entropy within these systems and only one crystallographic site for each M, A, and X element.[12]

All MAX phases, including the o-MAX phases, have the same space group i.e. $P6_3/mmc$ (#194). Most recently, we have revealed a new family of *in-plane* chemically ordered quaternary MAX phases, which we coined *i*-MAX.[13,14] The first material reported was $(Mo_{2/3}Sc_{1/3})_2AlC$, which not only displayed distinct Sc chains within the Mo-dominated M layer, but also allowed selective etching of Al as well as Sc to form a novel 2D MXene with ordered divacancies, resulting in elevated conductivity as well as supercapacitance.[13] This discovery was followed by $(Mo_{2/3}Y_{1/3})_2AlC$ and $(V_{2/3}Zr_{1/3})_2AlC$. All three *i*-MAX phases were described as monoclinic and suggested to belong to space group C2/c (#15).

Cr-based MAX phases, such as Cr_2AlC, are highly interesting for, e.g., high erosion resistance, damage tolerance, and self-healing capabilities.[15,16] Furthermore, these phases have to a large extent served as model systems for alloying to obtain various magnetic properties, evidenced from $(Cr,Mn)_2AlC$,[17,18] $(Cr,Mn)_2GeC$,[19] and $(Cr,Mn)_2GaC$,[20,21] see also Ref. 22 and references therein. Motivated by this, we here explore novel *i*-MAX phases based on Cr. Two new phases, $(Cr_{2/3}Sc_{1/3})_2AlC$ and $(Cr_{2/3}Y_{1/3})_2AlC$, are synthesized and analyzed with respect to structure by analytical high resolution scanning transmission electron microscopy (A-HRSTEM), X-ray diffraction (XRD), and Rietveld refinement. These results are expanded by first principle calculations based on density functional theory (DFT), investigating the magnetic ground state, dynamical stability, as well as mechanical properties.

2. EXPERIMENTAL DETAILS

For synthesis of $(Cr_{2/3}Sc_{1/3})_2AlC$ and $(Cr_{2/3}Y_{1/3})_2AlC$, elemental powders of graphite (99.999%), Cr (99.5%), Y (99.5%), (Sigma-Aldrich), Al (99.8%, ALFA AESAR) and Sc (99.99%, Stanford Advanced Material) with mesh sizes of -200, -100, -40, -200 and -200 were used. After mixing stoichiometric ratios of the powders in an agate mortar, the mixed powders were placed in a covered Al_2O_3 crucible, inserted in a tube vacuum furnace, heated at a rate of 10 ºC per minute up to 1400 ºC, and kept at that temperature for 2 h. The sintering was performed under constant Ar flow. After cooling down to room temperature in the furnace, the sintered samples were crushed and mixed, resulting in fine $(Cr_{2/3}Sc_{1/3})_2AlC$ and $(Cr_{2/3}Y_{1/3})_2AlC$ powders.

Phase identification was performed by XRD in a PANalytical X'Pert powder diffractometer, with Cu-K_α radiation (λ~1.54Å). A 1/4º divergent and 1/2º anti-scattered slit on the incident beam side, and a 5 mm anti-scatter slit together with a Soller slit (with an opening rad. of 0.04) on the diffracted beam side, were used for the measurements. θ-2θ scans were recorded between 5º and 120º in a continuous mode with a step size of 0.008º and a step dwell time of 40 s. The scans were analyzed by Rietveld refinement using the FULLPROF code.[23] The fitting parameters used in the program were the scale factors, 6 backgrounds parameters, *X* and *Y* profile parameters to limit the peak width to the major phase, lattice parameters, atomic positions and occupancies for all phases, and the overall B-factor for the main phase.

The atomic structure analysis was carried out by HRSTEM with the Linköping double Cs corrected FEI Titan^3 60–300 operated at 300 kV, equipped with a Super-X EDX system. The chemical composition of the samples was also measured by EDX in Leo 1550 Gemini with Oxford INCA EDX. Selected area electron diffraction (SAED) characterization was carried out using a FEI Tecnai G2 TF20 UT instrument operated at 200 kV. TEM powder specimens were prepared by dispersing a small amount of powder sample onto a carbon film grid.

3. COMPUTATIONAL DETAILS

All calculations were carried out using density functional theory (DFT) as implemented in the Vienna Ab Initio Simulation Package (VASP), combined with the projector augmented wave method.[24,25] The exchange-correlation potential was modeled by the Perdew-Burke-Ernzerhof generalized gradient approximation (PBE-GGA).[26] The 0 K energy was calculated for nonmagnetic (NM), ferromagnetic (FM), and antiferromagnetic (AFM) spin configurations of $(Cr_{2/3}Sc_{1/3})_2AlC$ and $(Cr_{2/3}Y_{1/3})_2AlC$. Several different AFM states were evaluated, some of

which required supercells, see **Supplemental Fig. 1**. For the NM and FM states, the convergence criterion of 0.1 meV/atom was reached using a 5x13x7 Monkhorst-Pack *k*-point grid, whereas the grid size for the AFM configurations varied depending on supercell size. The plane wave cutoff energy was 400 eV in all cases. To obtain the phonon dispersion relation, the finite displacement method[27] was used. The Phonopy software package[28] was used for generating the displacements as well as to obtain the force constants from the Hessian matrices determined by VASP. Sufficient convergence was reached for 1x2x1 supercells and 3x3x3 Monkhorst–Pack *k*–point grids.

For evaluation of mechanical properties, the Voigt (V) and Reuss (R) bulk ($B_{V,R}$), shear ($G_{V,R}$), and Young's ($E_{V,R}$) moduli of orthorhombic and monoclinic crystals can be expressed as

$$B_V = \frac{1}{9}(C_{11} + C_{22} + C_{33}) + \frac{2}{9}(C_{12} + C_{13} + C_{23}), \quad (1.1)$$

$$B_R = \frac{1}{(S_{11} + S_{22} + S_{33}) + 2(S_{12} + S_{23} + S_{13})}, \quad (1.2)$$

$$G_V = \frac{1}{15}((C_{11} + C_{22} + C_{33} - C_{12} - C_{13} - C_{23}) + 3(C_{44} + C_{55} + C_{66})), \quad (1.3)$$

$$G_R = \frac{15}{4(S_{11} + S_{22} + S_{33}) - 4(S_{12} + S_{23} + S_{13}) + 3(S_{44} + S_{55} + S_{66})}, \quad (1.4)$$

$$E_{V,R} = \frac{9B_{V,R}G_{V,R}}{(3B_{V,R} + G_{V,R})}. \quad (1.5)$$

The compliance constants S_{ij} can be found by taking the inverse of the elastic-constant matrix containing the elastic constants C_{ij}, i.e., $\boldsymbol{S} = \boldsymbol{C}^{-1}$. For an orthorhombic crystal, there are nine independent elastic constants: C_{11}, C_{22}, C_{33}, C_{44}, C_{55}, C_{66}, C_{12}, C_{13}, and C_{23}. A monoclinic lattice has four additional constants: C_{15}, C_{25}, C_{35}, and C_{46}. In this work, the elastic constants were calculated using the strain-energy method described in Ref. 29, with strain parameters ε = 0, ±0.1, and ±0.2.

4. RESULTS AND DISCUSSION

4.1 Structural analysis of $(Cr_{2/3}Y_{1/3})_2AlC$:

Phase identification of the sample with nominal $(Cr_{2/3}Y_{1/3})_2AlC$ composition was initially performed by XRD and the results are displayed in **Fig. 1**. According to Rietveld refinement, see **Supplementary Table 1**, the sample is composed of 60.77 wt% $(Cr_{2/3}Y_{1/3})_2AlC$ (space group *Cmcm* (#63)), with identified impurity phases being Y_2O_3, $(Cr_{2/3}Y_{1/3})_2AlC$ (space group C2/c (#15)) and Cr_2AlC MAX phase (#194) with weight percentages of 24.62, 8.54, and 6.06 wt%, respectively. The total χ^2 for this refinement is 4.25. The choice of phases tested in the refinement procedure is motivated by the SAED and HRSTEM presented below.

Fig. 2 shows a group of SAED patterns from single phase grains of space group #63 $(Cr_{2/3}Y_{1/3})_2AlC$. The first three SAED patterns in **Fig. 2(a-c)** have the same reflections 002 along the vertical direction but with successive tilting angle of 30˚. Except for the first pattern

in **Fig. 2(a)**, rest of the patterns cannot be indexed by the simple MAX phase 211 structure. Based on results presented below, the figure is indexed based on orthorhombic symmetry.

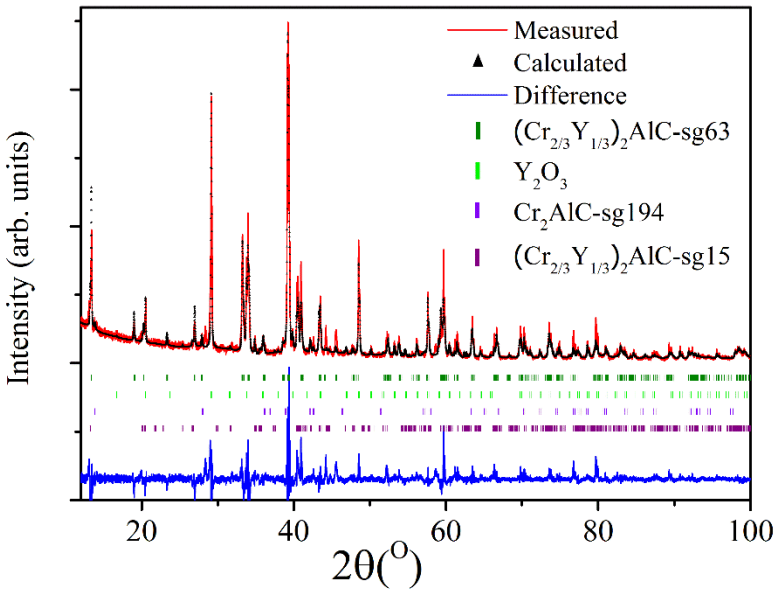

Fig. 1 Symmetric θ-2θ X-ray diffractogram for $(Cr_{2/3}Y_{1/3})_2AlC$. The measured scan (red), the calculated (black) scan using Rietveld refinement, and their difference (blue) are shown. Also plotted in the figure are the Bragg positions of the main phase followed by all the impurity phases identified in the sample.

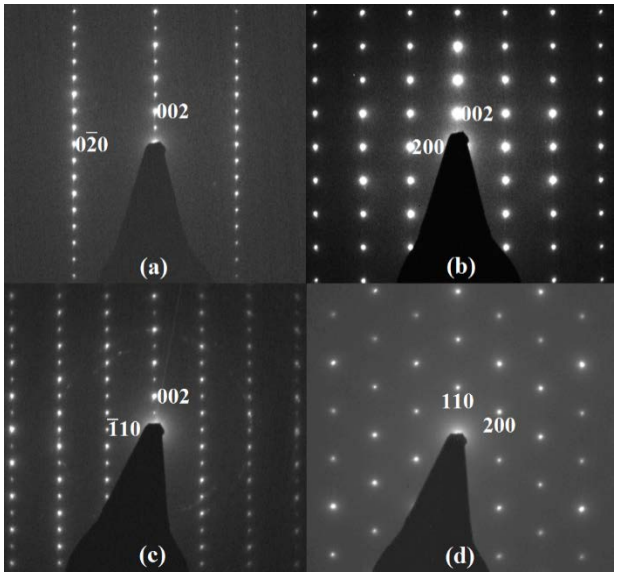

Fig. 2 SAED patterns from $(Cr_{2/3}Y_{1/3})_2AlC$, indexed using orthorhombic structure and space group Cmcm (#63) along (a) [100], (b) [010], (c) [110] and (d) [001].

To explore this new crystal structure, HRSTEM investigation was carried out to acquire high resolution Z-contrast images along the zone axes by using a high angle annular dark field (HAADF) detector, see **Fig. 3**. The brightest dots in the images correspond to Y and the grey dots to Cr, as Y is heavier than Cr. Al exhibits low contrast and C is too light to be visible. In **Fig. 3(a)**, all Y and Cr atoms are superimposed on each other, while from other three directions, **Fig. 3(b-d)**, Y, Cr, and Al are visually distinguishable. We initially use the notation of a MAX 211 structure. As can be seen in **Fig. 3(b, c)**, an interesting structural character is that Y and Cr atoms are ordered along [10-10] and [01-10] (in the Cr-Y plane) with an order of …YCrCrYCrCrY…., which is consistent with an *i*-MAX phase. This is not evident from the [11-20] direction, **Fig. 3(a)**, resembling the traditional 211 MAX structure. Thus, *in-plane* chemical order is evident, with the $Cr_{2/3}Y_{1/3}$ layer being composed of Y atoms at the center of hexagon of which the vertices are occupied by Cr atoms, see schematic in **Supplemental Fig. 2a.** The Cr-Y atomic network in adjacent layers (across the C layer) shifts along <11-20> and altogether result in an in-plane chemically ordered transition metal carbide sheet. Most notably, the Y atoms extend from the Cr network towards the Al layer, leading to an Al atom rearrangement. The latter is evident from every second Al position in **Fig. 3(c)**, closest to Y, being hardly visible (compare to **Fig. 3(a)**). Note that the metal atoms in the layers closest to Al, i.e., layer II and III in **Fig. 3c,d)**, have the same in-plane coordinates, while the second closest layers, i.e., layer I and IV, can be arranged differently, which is decisive of the crystal structure.

Focusing on the $(Cr_{2/3}Y_{1/3})_2C$ sheets in **Fig. 3(c)**, we can see that the Y and Cr atoms in different sheets have the same in-plane coordinates. Still, to get the atomic positions in the direction perpendicular to the paper, the atomic structure shown in **Fig. 3(d)** is obtained after tilting 60 degrees around the out-of-plane axis. The resulting Z-contrast image reveals that the atoms in layer II and III have the same in-plane coordinates, while the atoms in layer I and IV are shifted $a_0/2$ with respect to the atoms in layers II or III (where a_0 is the unit lattice parameter a or b of the traditional hexagonal structure of the MAX phase). As mentioned above, the Al layer does not display a uniform Al atomic distribution, with the Al atomic columns close to Cr exhibiting higher contrast than those close to Y, see **Fig. 3 (c,d).** The former Al columns are more Al dominant, i.e. of a higher Al concentration. On the other hand, viewed from [100] direction, Al atoms arrange uniform (see Fig. 3(a)). Thus, Al atoms form a Kagomé pattern in A layer, which is different from the Al atoms in traditional MAX structure, see **Supplemental Fig. 2b**. The preliminary coordinates of Cr, Y, and Al were obtained from the Z-contrast images, also inspired by previously suggested atomic arrangement of Mo-based *i*-MAX.[13,14] The suggested final atomic coordinates and cell parameters were gained from XRD Rietveld refinement (Supplementary **Table 1**). Apart from the Kagomé-like Al layer, the XRD refinement also suggests that in the Y position, there is a trace of Cr with occupancy of 0.25, for an occupancy of Y of 0.75. This partial intermixing cannot be observed in the STEM images. Compared with the traditional MAX phase structure, this *i*-MAX structure has no in-plane six fold symmetry (instead two-fold) along c axis, see **Fig. 3(b)**, though still exhibiting mirror symmetry with respect to a plane perpendicular to the a and b axes. Thus, the structure can be described as orthorhombic, with lattice parameters $a = 3a_0 = 9.337$ Å, $b = \sqrt{3}a_0 = 5.355$ Å and $c = c_0 = 13.219$ Å, and belonging to space group Cmcm (#63). By using this crystal structure model, the SAED patterns were indexed as shown in **Fig. 2**. The atomic structure image acquired along the 001 zone axis in **Fig. 3(b)**, and its projected 2D pattern of the structural model exhibited in the other insets of **Fig. 3**, are consistent. Although not identified from SAED and HRSTEM,

Rietveld refinement also showed indications of $(Cr_{2/3}Y_{1/3})_2AlC$ grains belonging to space group C2/c (#15). The obtained parameters for that phase is a = 8.926, b = 5.122, and c = 13.718 Å, with angles α = 90°, β = 102.837°, and γ = 90°.

Even though the Z contrast for Cr and Y differs significantly, evident from **Fig. 3**, allowing direct observation of the positions of these atoms, we have quantified the composition of an *i*-MAX grain of space group #63 by using Leo 1550 Gemini with Oxford INCA EDX. Local EDX measurements suggest Cr:Y:Al≈ 43.4(0.3):23.9(0.2):32.7(0.2), which is within error bars consistent with the theoretical ideal ratio of 44.4:22.2:33.3. No significant oxidation of $(Cr_{2/3}Y_{1/3})_2AlC$ was observed, with an oxygen content of less than 3 at% from EDX analysis.

The previously reported *i*-MAX phases have been suggested to belong to space group #15. Consequently, $(Cr_{2/3}Y_{1/3})_2AlC$ is the first *i*-MAX phase, which due to the stacking sequences of the M-C-M layers can be described by space group #63. However, it should be stressed that all M-C-M layers are equivalent upon potential removal of Al and delamination into free-standing sheets. As there are no MXenes (the 2D derivative of MAX phases) to date based on Cr, the here presented finding may realize such 2D materials.

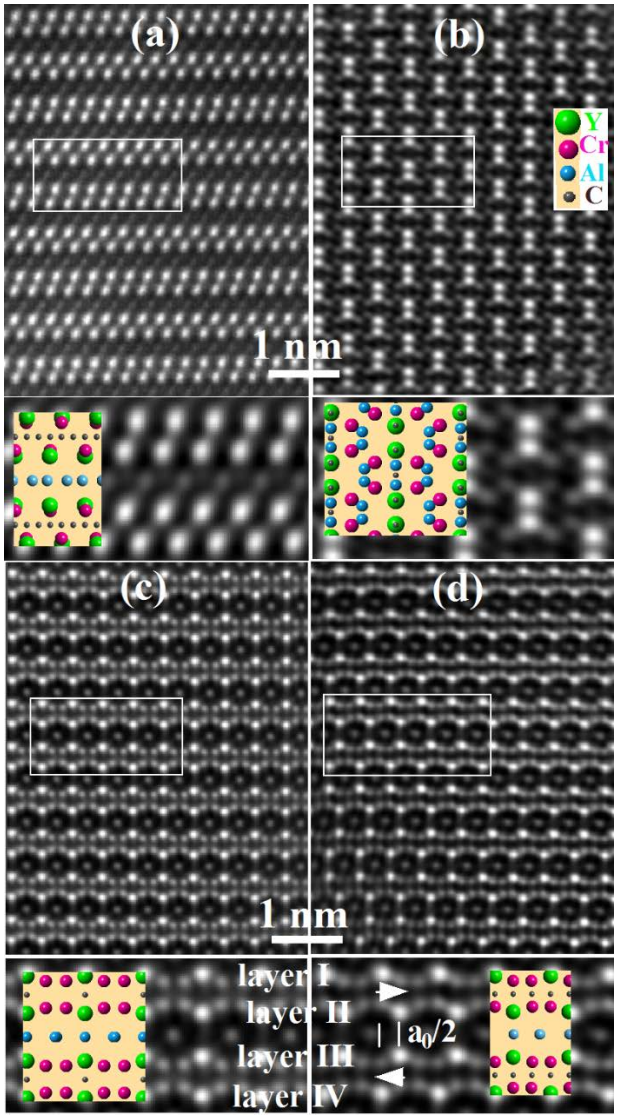

Fig. 3 Z-contrast images of $(Cr_{2/3}Y_{1/3})_2AlC$ along (a) [100], (b) [001], (c) [010], and (d) [110], respectively.

4.2 Structural analysis of $(Cr_{2/3}Sc_{1/3})_2AlC$:

Motivated by the realization of a new *i*-MAX phase based on *M*= Cr and Y, the same experimental procedure was applied for *M*= Cr and Sc. Phase analysis from XRD and Rietveld refinement, see **Fig. 4** and **Supplementary Table 2**, was inspired by the SAED and HRSTEM results presented below. The majority of the sample (85.1 *wt.%*), contained $(Cr_{2/3}Sc_{1/3})_2AlC$ (space group C2/c (#15)), with cell parameters of a = 9.069, b = 5.246, and c = 13.210 Å, with angles α = 90°, β = 103.408, and γ = 90°. The impurity phases obtained in the refinement were $(Cr_{2/3}Sc_{1/3})_2AlC$ (space group *Cmcm* (#63)) and Cr_2Al with a weight percentage of 9.8 and 5.1, respectively. The former has cell parameters of a = 9.297, b = 5.414, and c = 13.012 Å with angles $\alpha = \beta = \gamma = 90°$. The total χ^2 is 3.62, and the refinement also reveals a slight Cr-Sc intermixing in the Cr positions.

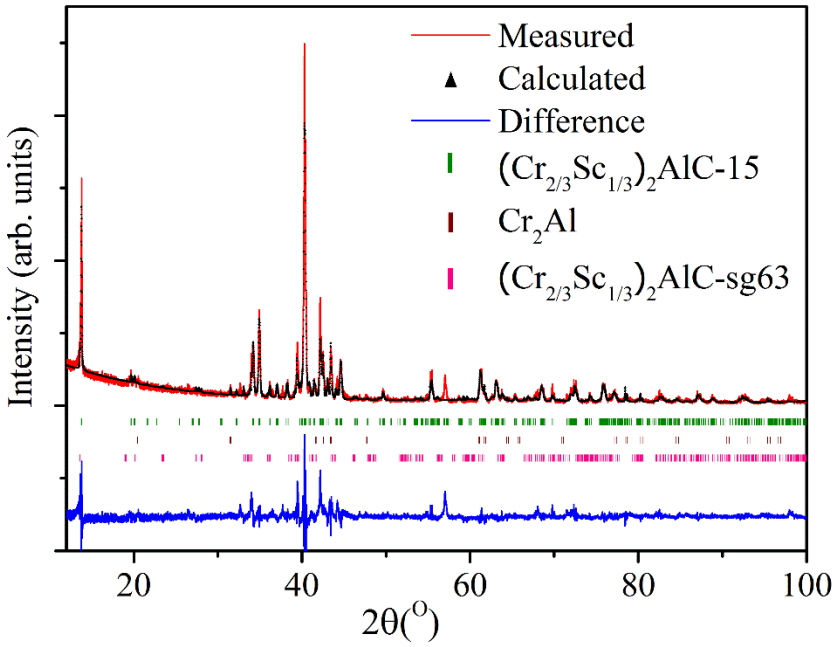

Fig. 4 Symmetric θ-2θ X-ray diffractogram for $(Cr_{2/3}Sc_{1/3})_2AlC$. The measured scan(red), the calculated (black) scan using Rietveld refinement, and their difference (blue) are shown. Also plotted in the figure are the Bragg positions of the main phase and all the impurity phases identified in the sample.

The SAED patterns from *i*-MAX $(Cr_{2/3}Sc_{1/3})_2AlC$ grains are shown in **Fig. 5**. The three patterns to the left, **Fig. 5(a-c)**, are acquired from single-phase grains of $(Cr_{2/3}Sc_{1/3})_2AlC$ showing an orthorhombic *i*-MAX structure equivalent to the one identified for $(Cr_{2/3}Y_{1/3})_2AlC$, as discussed above. The SAED patterns in **Fig. 5(a-c)** are consequently indexed and labelled accordingly. The structure is also confirmed by HRSTEM, exemplified in **Supplementary Fig. 3**.

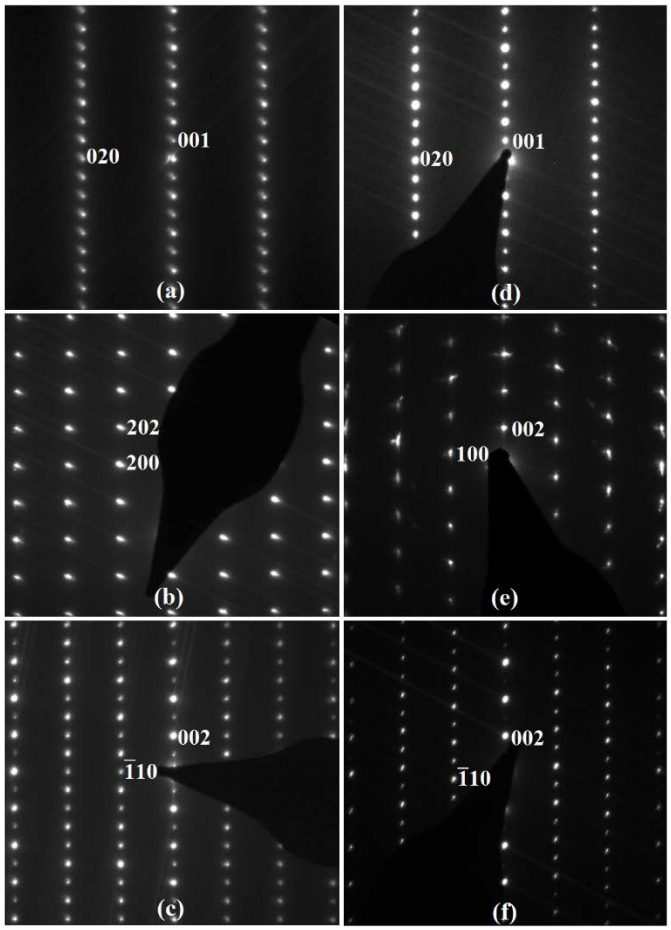

Fig. 5 SAED patterns from $(Cr_{2/3}Sc_{1/3})_2AlC$ grains of (a-c) orthorhombic along (a) [100], (b) [010], (c) [110]; and (d-f) monoclinic structure, along (a) [100], (b) [010], (c) [110].

The SAED patterns to the right, **Fig 5(d-f)**, are obtained from equivalent single phase $(Cr_{2/3}Sc_{1/3})_2AlC$ grains with the same axis in the vertical direction. The SAED pattern in **Fig. 5(d)** is the same as that in **Fig. 5(a)**, however, **Fig. 5(e,f)** differ from **Fig. 5(b,c)**, which indicates different crystal structures. Again, HRSTEM was utilized to resolve the details of the crystal structure in **Fig 5(d-f)**, with the Z-contrast images shown in **Fig. 6**. **Fig. 6(a)** looks equivalent to **Fig. 3(a)**, which also looks similar to the traditional 211 MAX phase structure along the [11-20] direction. Consequently, this orientation cannot be used for structural identification here. HRSTEM images obtained from tilting the grain 30˚ or -30˚ are shown in **Fig. 6(b,c)**, resolving the previously superimposed Cr and Sc. The Z-contrast images, however, only produce a minor contrast difference between the Cr and Sc atoms (Cr slightly brighter) due to similar mass. However, an *in-plane* chemical ordering in the form of …ScCrCrScCrCrSc… can be distinguished. In this new *i*-MAX structure, layer II and III display the same in-plane atomic coordinates, while the atom positions in layers I and IV appear to be different. Expressed in hexagonal MAX phase symmetry, it can be seen in **Fig. 6(b)** that the atoms in layer I has shifted $a_0/2$ with respect to layer II along $[11\bar{2}0]$. The same shift exists also between the layer III and

layer IV, and shift direction can be along $[\bar{1}\bar{1}20]$ or $[1\bar{2}10]$. **Fig. 6(c)** reveals that the atoms in layer IV has shifted $a_0/2$ along $[1\bar{2}10]$, rather than $[\bar{1}\bar{1}20]$ with respect to layer III. Keep in mind, layer II and layer III have the same in-plane atomic coordinates, and the rotation angle between $[11\bar{2}0]$ and $[\bar{1}\bar{1}20]$ is 120˚. Thus, there is a 120˚ rotation between the otherwise equivalent atomic arrangements in layer I and IV, and consequently a 120˚ rotation between the adjacent sub-lattices. This is consistent with the atomic arrangement observed in **Fig. 6(c)**. Thus, a monoclinic *i*-MAX phase is evident, which can be described by space group C2/c (#15) and the lattice parameters $a=3a_0$, $b=\sqrt{3}b_0$, $c=(c_0^2 + (\frac{1}{3}a_0^2))^{1/2}$, and $\gamma=90^\circ + \arctan(a_0/(c_0^2 + (0.5a_0)^2)^{1/2} = 103^\circ$, where a_0, b_0 and c_0 are the cell parameters of the traditional 211 MAX phase.

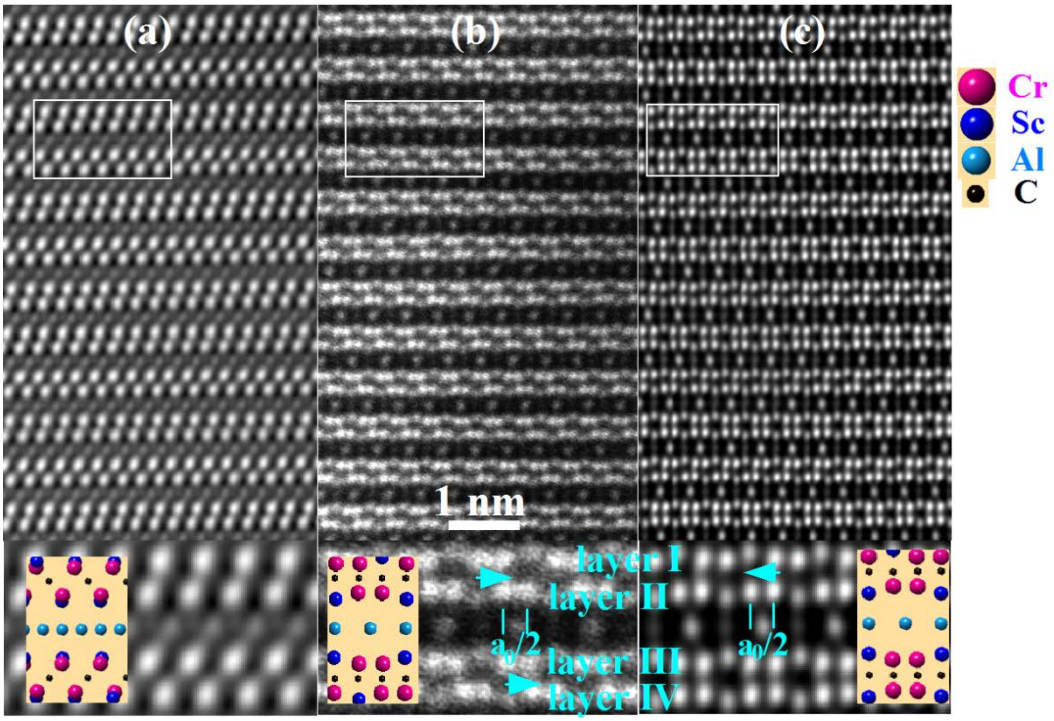

Fig. 6 STEM images of $(Cr_{2/3}Sc_{1/3})_2AlC$-sg15 along (a) [100], (b) [010], and (c) [110]

Similar to the orthorhombic i-MAX structure, the Al atomic arrangement in the monoclinic $(Cr_{2/3}Sc_{1/3})_2AlC$ structure is redistributed as compared to a traditional 211 MAX phase, resulting in brighter Al dots close to Cr and darker (hardly visible) Al dots close to Sc, as shown in **Figs. 6(b, c)**. The preliminary cell parameters and atomic coordinates obtained from SAED and STEM were refined by using XRD and Rietveld refinement as presented above (**Fig. 4** and **Supplementary Table 2)**.

To quantify the local composition with respect to Cr, Sc, and Al content in $(Cr_{2/3}Sc_{1/3})_2AlC$ (#15) grains, EDX measurements was carried out, showing a Cr:Sc:Al ratio of approximately 44.5(0.2):21.6(0.1):33.9(0.2). No oxygen signal was observed in the sample.

Finally, it should be stressed that the here identified space groups of both $(Cr_{2/3}Sc_{1/3})_2AlC$ and $(Cr_{2/3}Y_{1/3})_2AlC$ are based on an atomic stacking which yield equivalent M-C-M layers if

delaminated upon removal of Al or Al+Sc/Y. This is important for future potential processing of Cr-based MXenes, which may be realized from the here presented *i*-MAX phases.

4.3 Magnetic ground state (0 K) of $(Cr_{2/3}Y_{1/3})_2AlC$ and $(Cr_{2/3}Sc_{1/3})_2AlC$

Previous work has shown the importance of choice of method for treating electron correlation effects in multicomponent carbides, as well as choice of spin configuration (requiring supercell formalism) for identification of the magnetic ground state.[30,31] Therefore we have evaluated nonmagnetic, FM, and several AFM spin configurations, see **Supplementary Fig. 1**. The here presented AFM state, denoted AFM$[0001]^{X}_{4}$, is shown in **Fig. 7** and should be read as the Cr moments being parallel over four consecutive *M* layers, and then change sign upon crossing an *X* layer. The other AFM configurations investigated have higher energy than AFM$[0001]^{X}_{4}$, and since ordering similar to AFM$[0001]^{X}_{4}$ is implicated in at least one other MAX phase, Mn_2GaC,[32,33] we have chosen to here include only this configuration. For all spin configurations, we have calculated the 0 K energies, lattice parameters and local magnetic moments of orthorhombic (*Cmcm*, #63) and monoclinic (*C*2/*c*, #15) $(Cr_{2/3}Sc_{1/3})_2AlC$ and $(Cr_{2/3}Y_{1/3})_2AlC$. The results are displayed in **Table 1 and 2**.

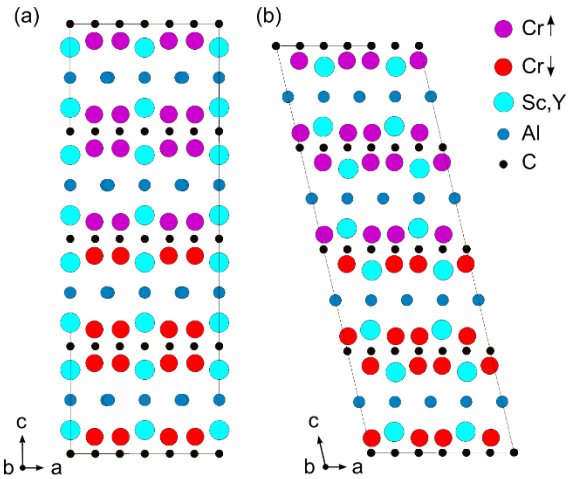

Fig. 7 1x1x2 supercells of $(Cr_{2/3}M_{1/3})_2AlC$ (M=Sc or Y) in the AFM$[0001]^{X}_{4}$ magnetic state for space groups (a) *Cmcm* and (b) *C*/2*c*.

Table 1. Energy, magnetic state, and average local moments of $(Cr_{2/3}Sc_{1/3})_2AlC$ and $(Cr_{2/3}Y_{1/3})_2AlC$. E-E_{NM} is the difference in energy relative to the nonmagnetic configuration.

Phase	Space group	Magnetic state	Energy (ev/atom)	E-E_{NM} (meV/fu)	Avg. local moment (μ_B/Cr)
$(Cr_{2/3}Sc_{1/3})_2AlC$	*Cmcm* (#63)	NM	-7.910	0	0
		FM	-7.912	−6	0.63
		AFM$[0001]^{X}_{4}$	-7.911	−4	0.60
	*C*2/*c* (#15)	NM	-7.910	0	0

		FM	-7.912	−7	0.63
		AFM[0001]$^{X}_{4}$	-7.911	−4	0.52
$(Cr_{2/3}Y_{1/3})_2AlC$	*Cmcm* (#63)	NM	-7.867	0	0
		FM	-7.870	−15	0.76
		AFM[0001]$^{X}_{4}$	-7.871	−15	0.85
	*C*2/*c* (#15)	NM	-7.867	0	0
		FM	-7.872	−17	0.81
		AFM[0001]$^{X}_{4}$	-7.870	−15	0.88

Table 2. Calculated lattice parameters of $(Cr_{2/3}Sc_{1/3})_2AlC$ and $(Cr_{2/3}Y_{1/3})_2AlC$.

Phase	Space group	Magnetic state	Lattice parameter (Å)		
			a	b	c
$(Cr_{2/3}Sc_{1/3})_2AlC$	*Cmcm* (#63)	NM	9.090	5.199	12.814
		FM	9.103	5.216	12.816
		AFM[0001]$^{X}_{4}$	9.105	5.213	12.804
	*C*2/*c* (#15)	NM	9.029	5.232	13.181
		FM	9.052	5.241	13.181
		AFM[0001]$^{X}_{4}$	9.047	5.243	13.170
$(Cr_{2/3}Y_{1/3})_2AlC$	*Cmcm* (#63)	NM	9.320	5.322	13.159
		FM	9.303	5.338	13.189
		AFM[0001]$^{X}_{4}$	9.326	5.346	13.169
	*C*2/*c* (#15)	NM	9.247	5.358	13.532
		FM	9.269	5.368	13.552
		AFM[0001]$^{X}_{4}$	9.276	5.371	13.538

Table 1 shows that for each compound, the energies of the NM and magnetic states in the *Cmcm* space group are degenerate in energy with the corresponding states in the *C*/2*c* space group. Moreover, for a given compound and space group, the FM and AFM[0001]$^{X}_{4}$ states are degenerate (or very close to) in energy, and significantly lower in energy than the NM state. The energy difference between the FM and NM state, (E_{FM}-E_{NM}), and the AFM[0001]$^{X}_{4}$ and NM state, (E_{X4}-E_{NM}), for both compounds is comparable to the energy difference of −11 meV/fu between the theoretically identified lowest-energy magnetic state (AFM) and the NM state of Cr_2AlC.[30] The calculations thus suggest that the compounds have some magnetic ordering. It should be noted, however, that they do not give a clear indication as to whether the FM or the AFM[0001]$^{X}_{4}$ magnetic state is more likely to be the 0 K ground state. Furthermore,

it cannot be ruled out that possible other, more complex, magnetic spin configurations not evaluated here, would lower the energy of the system even further.

The magnetism in $(Cr_{2/3}Sc_{1/3})_2AlC$ and $(Cr_{2/3}Y_{1/3})_2AlC$ (independent on simulated space group) arises primarily from localized Cr moments, see Table 1, ranging in magnitude from 0.52 to 0.88 μ_B/Cr, which is similar to the calculated local moments of 0.70 μ_B/Cr in Cr_2AlC.[30] The induced magnetic moments of the other atoms in the two alloys are smaller than the Cr moments by at least an order of magnitude. Another observation is that the Cr moments in $(Cr_{2/3}Y_{1/3})_2AlC$ are higher than in $(Cr_{2/3}Sc_{1/3})_2AlC$, regardless of the space group used in the simulations. Also, in $(Cr_{2/3}Y_{1/3})_2AlC$ the Cr moments in the AFM$[0001]_4^X$ state are higher than in the FM state, whereas the opposite is found for $(Cr_{2/3}Sc_{1/3})_2AlC$.

It is evident from **Table 2** that the magnetic configuration does not significantly change the calculated lattice parameters. Still, the parameters suggested by the XRD refinement of $(Cr_{2/3}Sc_{1/3})_2AlC$ in both C2/c and Cmcm as well as $(Cr_{2/3}Y_{1/3})_2AlC$ in Cmcm structures (see **Supplementary Tables 1 and 2**, are consistent with the calculated results (see **Table 2**).

We have also calculated the dynamical stability, i.e. the stability of the material with respect to lattice vibrations, of the NM and FM states for both compounds and space groups, as shown in **Supplementary Fig. 3**. The phonon dispersions show that all frequencies are positive, and consequently $(Cr_{2/3}Sc_{1/3})_2AlC$ as well as $(Cr_{2/3}Y_{1/3})_2AlC$ can be concluded dynamically stable.

4.4 Calculated mechanical properties of $(Cr_{2/3}Y_{1/3})_2AlC$ and $(Cr_{2/3}Sc_{1/3})_2AlC$

The Voigt and Reuss moduli of NM, FM, and AFM$[0001]_4^X$ $(Cr_{2/3}Sc_{1/3})_2AlC$ and $(Cr_{2/3}Y_{1/3})_2AlC$ are listed in **Table 3**, together with the Voigt–Reuss–Hill averages, which are the arithmetic means of the moduli taken over their Voigt and Reuss values.

Table 3. The Voigt (V), Reuss (R), and Voigt-Reuss-Hill (VRH) bulk (B), shear (G) and Young´s (E) moduli of $(Cr_{2/3}Sc_{1/3})_2AlC$ and $(Cr_{2/3}Y_{1/3})_2AlC$.

Phase	Space group	Magnetic state	B_V (GPa)	B_R (GPa)	B_{VRH} (GPa)	G_V (GPa)	G_R (GPa)	G_{VRH} (GPa)	E_V (GPa)	E_R (GPa)	E_{VRH} (GPa)
$(Cr_{2/3}Sc_{1/3})_2AlC$	*Cmcm*	NM	150	150	150	123	102	112.5	290	249	269.5
	(#63)	FM	148	148	148	124	104	114	291	252	271.5
		AFM$[0001]_4^X$	138	137	137.5	122	102	112	282	245	263.5
	*C*2/*c*	NM	152	122	137	104	97	100.5	253	230	241.5
	(#15)	FM	142	114	128	104	98	101	251	229	240
		AFM$[0001]_4^X$	139	119	129	103	99	101	248	232	240
$(Cr_{2/3}Y_{1/3})_2AlC$	*Cmcm*	NM	138	138	138	116	96	106	271	233	252
	(#63)	FM	136	135	135.5	117	97	107	272	235	253.5
		AFM$[0001]_4^X$	147	144	145.5	119	94	106.5	282	233	257.5
	*C*2/*c*	NM	139	81	110	97	83	90	237	186	211.5
	(#15)	FM	136	36	86	100	62	81	240	117	179
		AFM$[0001]_4^X$	134	85	109.5	99	84	91.5	238	189	213.5

As seen in the table, a substitution of Y for Sc generally leads to a decrease of the modulus, while a change of space group affects only the theoretical shear and Young's moduli, which decrease in going from an orthorhombic (*Cmcm)* to a monoclinic (*C*2/*c*) lattice description. The magnetic state, on the other hand, has little impact on any of the three moduli, as expected based on the non-significant structural change between different magnetic configurations. Further, we note that, for *C*2/*c* FM $(Cr_{2/3}Y_{1/3})_2AlC$, all Reuss moduli are anomalously small compared to the Voigt moduli. This can be traced back to small computational errors in the calculations of some of the elastic constants, which in this particular case have combined in such a way as to create large systematic errors in the Reuss moduli. Another observation is that for space group *Cmcm*, the Reuss bulk modulus for a given compound and magnetic state is virtually unchanged compared to the Voigt bulk modulus, whereas it decreases for space group *C*2/*c*. For the shear and Young's moduli, on the other hand, the Reuss values are lower than the Voigt values regardless of space group.

The Voigt bulk moduli calculated here, which range in magnitude from 134 to 152 GPa, can be put in relation to the Voigt bulk moduli of NM and in-AFM1 (the theoretical lowest-energy magnetic state) of Cr_2AlC calculated in Ref. 30, which are 188 and 171 GPa, respectively. Incorporation of 16.7 at. % Sc or Y thus clearly decreases the bulk modulus compared to the ternary Cr-based MAX phase.

Finally, we note that, for both space groups and all magnetic states, both compounds fulfill the criteria for mechanical stability, which state that a crystal structure is mechanically stable if and only if all eigenvalues of the elastic constant matrix are positive.[34] This has been checked using the eig function in MATLAB. The calculated elastic constants can be found in the Supplementary Table 3 and 4.

5. CONCLUSIONS

Two new Cr-based phases belonging to the family of *i*-MAX phases have been revealed: $(Cr_{2/3}Y_{1/3})_2AlC$, primarily described by an orthorombic structure of space group Cmcm (#63) and lattice parameters a = 9.337, b = 5.355, and c = 13.219 Å, and $(Cr_{2/3}Sc_{1/3})_2AlC$, predominantly given by monoclinic structure of space group C2/c (#15) and lattice parameters a = 9.069, b = 5.246, and c = 13.210 Å, with angles $\alpha = \gamma = 90°$ and $\beta = 103.408°$. Calculations based on Density Functional theory suggest dynamically and mechanically stable materials, and that ferro- and antiferromagnetic spin configurations significantly lower energy relative to the non-magnetic state.

Acknowledgements:
J.R. acknowledge support from the Swedish Foundation for Strategic Research (SSF) through the Synergy Grant FUNCASE. J.R. and L.H. also acknowledge support from the Knut and Alice Wallenberg (KAW) Foundation for a Scholar Grant, a Fellowship Grant, Project funding (KAW 2015.0043), and for support to the Linköping Ultra Electron Microscopy Laboratory. The Swedish Research council is gratefully acknowledged through Project 621-2012-4425, 2013-4018, and 642-2013-8020.

[1] Eerenstein, W.; Mathur, N. D.; Scott, J. F. *Nature* **2006,** *442* (7104), 759-765.
[2] Ghidiu, M.; Lukatskaya, M. R.; Zhao, M.-Q.; Gogotsi, Y.; Barsoum, M. W. *Nature* **2014,** *516* (7529), 78-81.
[3] Barsoum MW. Prog. *Solid State. Chem*. **2000**, *28*, 201-281.
[4] M.W. Barsoum. MAX Phases: Properties of Machinable Ternary Carbides and Nitrides, Wiley-VCH, Weinheim, 2013.
[5] Barsoum, M. W.; Zhen, T.; Kalidindi, S. R.; Radovic, M.; Murugaiah, A. *Nature Mater.* **2003,** *2* (2), 107-111.
[6] Gruber, J.; Lang, A. C.; Griggs, J.; Taheri, M. L.; Garritt, J.; Tucker,G. J.; Barsoum, M. W. *Scientific Reports* **2016**, *6*, 33451.
[7] Liu, Z.; Wu, E.; Wang, J.; Qian, Y.; Xiang, H.; Li, X.; Jin, Q.; Sun, G.; Chen, X.; Wang, J.; Li, M. *Acta Mater.* **2014**, *73*, 186-193.
[8] Caspi, E. N.; Chartier, P.; Porcher, F.; Damay, F.; Cabioc'h, T.; *Mater. Res. Lett.* **2015**, *3*, 100–106.
[9] Anasori, B, Halim J, Lu J, Voigt CA, Hultman L, and Barsoum MW, Scr. Mater. 101, 5 (2015).
[10] Anasori B.; Dahlqvist, M.; Halim, J.; Moon, E. J.; Lu, J.; Hosler, B. C.; Caspi, E. N.; May, S. J.; Hultman, L.; Eklund, P.; Rosen, J.; Barsoum, M. W. *J. of Appl. Phys*. **2015**, *118*, 094304.
[11] Meshkian, R.; Tao, Q. Z.; Dahlqvist, M.; Lu, J.; Hultman, L.; Rosen, J. *Acta Materialia* **2017**, *125*, 476–480.
[12] Dahlqvist, M.; Rosen, *Phys. Chem. Chem. Phys*. **2015**, *17*, 31810-31821
[13] Tao, Q. Z.; Dahlqvist, M.; Lu, J.; Kota, S.; Meshkian, R.; Halim, J.; Palisaitis, J.; Hultman, L.; Barsoum, M. W.; Persson, P. O. A.; Rosen, J. *Nature Communications*, 2017 8 14949.
[14] Dahlqvist, M.; Lu, J.; Meshkian, R.; Tao, Q. Z.; Hultman, L.; and Rosen, J. *Sci. Adv*. 2017 3 e1700642.
[15] Shen, L.; Eichner, D.; van der Zwaag, S.; Leyens, C.; Sloof, W. G. *Wear* **2016**, *358-359*, 1-6.
[16] Shang, L.; Baben, M. T.; Pradeep, K. G.; Sandlöbes, S.; Amalraj, M.; Hans, M.; Chang, K. K.; Music, D.; Primetzhofer, D.; Schneider, J. M. *J. of the European Ceramic Society* **2016**, *37*, 35-41.
[17] Mockute, A.; Dahlqvist, M.; Emmerlich, J.; Hultman, L.; Schneider, J. M.; Persson, P. O. Å.; Rosen, J. *Phys. Rev. B* **2013**, *87*, 094113.
[18] Mockute, A.; Persson, P. O. Å.; Magnus, F.; Ingason, A. S.; Olafsson, S.; Hultman, L.; Rosen, J. *Phys. Status Solidi RRL* **2014**, *8*, 420-423.
[19] Ingason, A. S.; Mockute, A.; Dahlqvist, M.; Magnus, F.; Olafsson, S.; Arnalds, U.; Alling, B.; Abrikosov, I.A.; Hjorvarsson, B.; Persson, P.O.Å.; Rosen, J. *Phys. Rev. Lett.* **2013**, *110*, 195502.
[20] Petruhins, A.; Ingason, A. S.; Lu, J.; Magnus, F.; Olafsson, S.; Rosen J. *J. Mater. Sci.* **2015**, *50***,** 4495-4502.
[21] Salikhov, R.; Semisalova, A. S.; Petruhins, A.; Ingason, A. S.; Rosen, J.; Wiedwald, U.; Farle, M. *Mater. Res. Lett*. **2015**, *3*, 156-160.
[22] Ingason, A. S.; Dahlqvist, M.; Rosen J. *J. Phys.: Condens. Matter* **2016**, *28* 433003.
[23] Rietveld, H.M. J. of Applied Crystallography **1969**, *2*, 65-71.
[24] Kresse, G.; Furthmüller, J. *Physical Review B*, **1996**, *54*, 11169-11186.
[25] Blöchl, P. E. *Physical Review B*, **1994**, *50*, 17953-17979.
[26] Perdew, J. P.; Burke, K.; Ernzerhof, M. *Physical Review Letters*, **1996**, *77*, 3865-3868.
[27] Gonze, X.; Lee, C. *Physical Review B*, **1997**, *55*, 10355-10368.

[28] Togo, A.; Oba, F.; Tanaka, I. *Physical Review B*, **2008**, *78*, 134106.
[29] Wang, J.; Sehitoglu, H. *International Journal of Plasticity*, **2014**, *61*, 17-31.
[30] Dahlqvist, M.; Alling, B.; Rosén, J. *J. Appl. Phys*. **2013**, *113*, 216103.
[31] Dahlqvist, M.; Alling, B.; Rosen, J. *J. of Physics Condensed Matter* **2015**, *27*, 95601-8.
[32] Dahlqvist, M.; Ingason, A. S.; Alling, B.; Magnus, F.; Thore, A.; Petruhins, A.; Mockute, A.; Arnalds, U. B.; Sahlberg, M.; Hjörvarsson, B.; Abrikosov I. A.; Rosen, J. *Physical Review B*, **2016**, *93*, 014410.
[33] Ingason, A. S.; Palsson, G. K.; Dahlqvist, M.; Rosen, J. *Physical Review B*, **2016**, *94*, 024416.
[34] Mouhat F and Coudert FX, *Physical Review B* 90 (2014) 224104.

Supporting information is available.
The contents of the material supplied:

1. Fig. S1 and figure caption.
2. Fig. S2 and figure caption.
3. Fig. S3 and figure caption.
4. Fig. S4 and figure caption.
5. Table S1: Structural information for $(Cr_{2/3}Y_{1/3})_2AlC$ from Rietveld refinement.
6. Table S2: Structural information for $(Cr_{2/3}Sc_{1/3})_2AlC$ from Rietveld refinement.
7. Table S3: Elastic constants (in GPa) for nonmagnetic (NM), ferromagnetic (FM), and antiferromagnetic ($AFM[0001]_4^X$) $(Cr_{2/3}Sc_{1/3})_2AlC$.
8. Table S4: Elastic constants (in GPa) for nonmagnetic (NM), ferromagnetic (FM), and antiferromagnetic (AFM[0001]X4) (Cr2/3Y1/3)2AlC.

For Table of Contents Use Only

Manuscript title: Theoretical and experimental exploration of a novel in-plane chemically-ordered $(Cr_{2/3}M_{1/3})_2AlC$ *i-MAX* phase with M=Sc and Y

Author list: Lu J*, Thore A, Meshkian R, Tao Q, Hultman L and Rosen J

TOC graphic, and synopsis:

Two laminated transition metal carbides, $(Cr_{2/3}Sc_{1/3})_2AlC$ and $(Cr_{2/3}Y_{1/3})_2AlC$ with in-plane chemical order have been discovered by STEM, SAED and X-ray diffraction Rietveld refinement. An orthorhombic structure of space group Cmcm (#63) and a monoclinic structure of space group C2/c (#15) are identified. The magnetic properties of those compounds were studied by theoretical calculation.

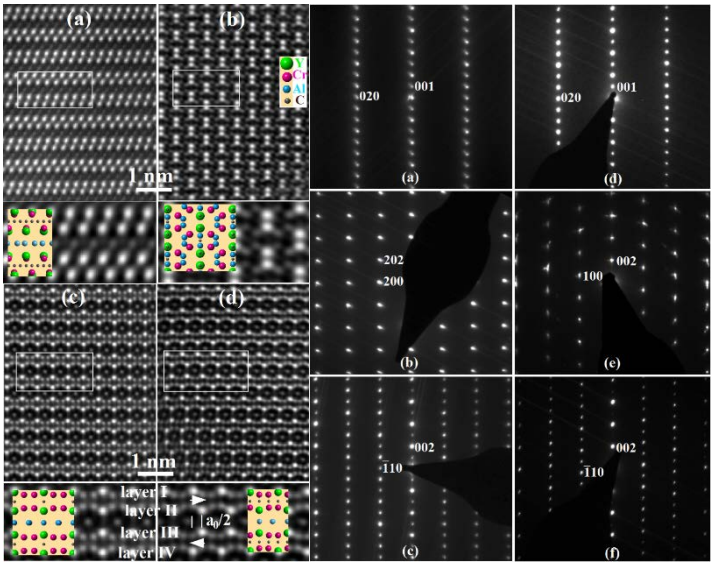
(a)
(b)
V
Cr
Al
C
1 nm
(c)
(d)
1 nm
layer I
layer II
layer III
layer IV
$a_0/2$
020
001
(a)
020
001
(d)
202
200
(b)
002
100
(e)
002
$\bar{1}10$
(c)
002
$\bar{1}10$
(f)

Theoretical and experimental exploration of a novel in-plane chemically-ordered $(Cr_{2/3}M_{1/3})_2AlC$ *i-MAX* phase with M=Sc and Y

Lu J*, Thore A, Meshkian R, Tao Q, Hultman L and Rosen J

Thin Film Physics, Department of Physics, Chemistry and Biology (IFM), Linköping University, SE-581 83 Linköping, Sweden

* junlu@ifm.liu.se

Supporting information

(SUPPLEMENTARY MATERIAL)

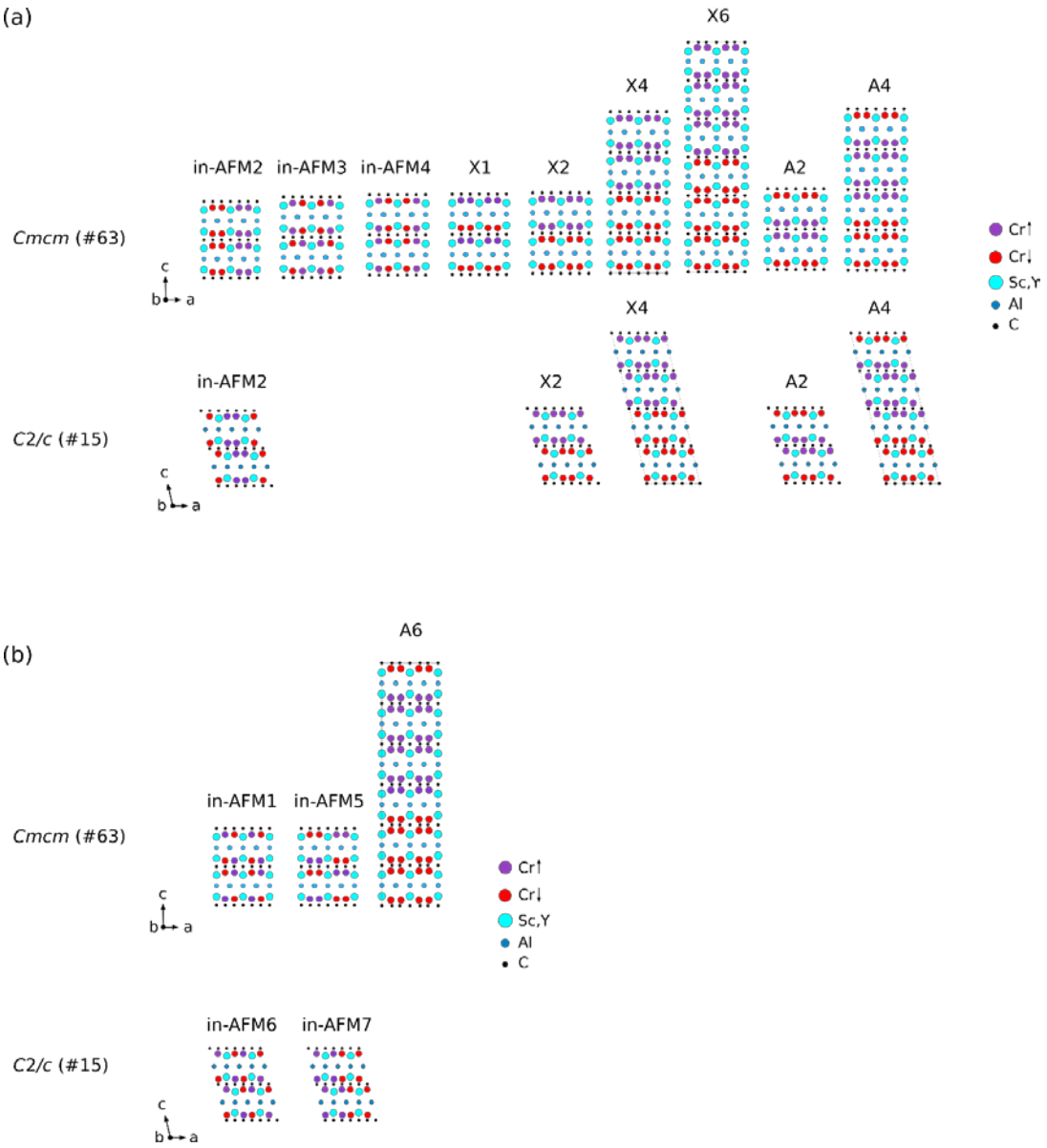

Figure S1. Evaluated antiferromagnetic states for $(Cr_{2/3}Sc_{1/3})_2AlC$ and $(Cr_{2/3}Y_{1/3})_2AlC$. (a) Fully relaxed states. Structural data and energies can be found in Tab. I and II in Supplementary Material. (b) Partially relaxed states. During relaxation, these states either moved towards a ferromagnetic or a nonmagnetic state, or were deemed too high in energy to be of interest.

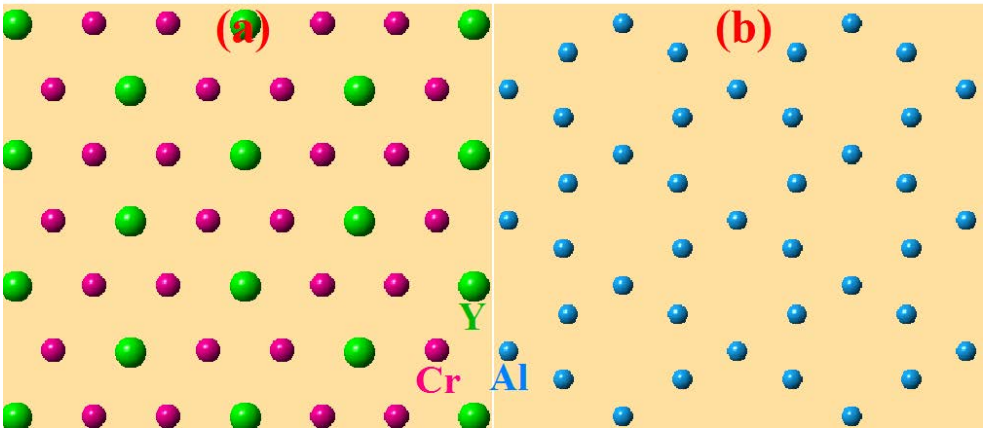

Figure S2: Top view of the *i*-MAX $(Cr_{2/3}Y_{1/3})_2AlC$ (a) *M* layer, where *in-plane* chemical order is given by the $Cr_{2/3}Y_{1/3}$ layer composed of Y atoms at the center of hexagon of which the vertices are occupied by Cr atoms, and (b) Al layer, showing a characteristic Kagomé-like structure.

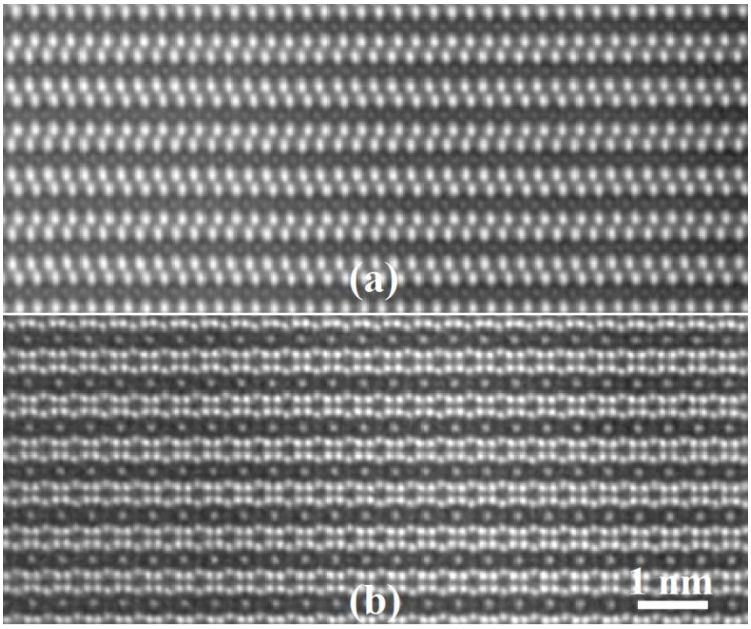

Figure. S3: HRSTEM images of $(Cr_{2/3}Sc_{1/3})_2AlC$ with space group Cmcm (#63), (a) along [100], and (b) along [010] orientation.

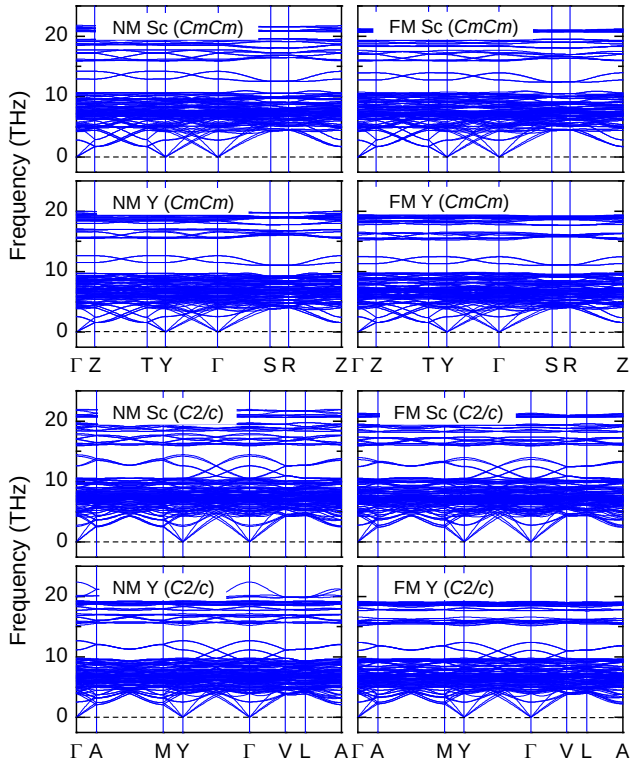

Figure S4. Phonon dispersion in nonmagnetic (NM) and ferromagnetic (FM) $(Cr_{2/3}Sc_{1/3})_2AlC$ and $(Cr_{2/3}Y_{1/3})_2AlC$ for space groups *Cmcm* and *C*/2*c*.

Table S1. Structural information for $(Cr_{2/3}Y_{1/3})_2AlC$ from Rietveld refinement.

Space group	*Cmcm* (#63)
a (Å)	9.33673
b (Å)	5.35495
c (Å)	13.21787
α	90.000
β	90.000
γ	90.000
Cr	16h (0.1652 0.8360 0.4263)
Y	8f (0.0000 0.3353 0.3801) Occupancy of Y = 1.744 and Cr = 0.256
Al	4c (0.0000 0.8249 0.2500) 8g (0.2466 0.0970 0.2500)
C	8e (0.1435 0.5000 0.0000) 4b (0.0000 0.0000 0.0000)

Table S2. Structural information for $(Cr_{2/3}Sc_{1/3})_2AlC$ from Rietveld refinement.

Space group	*C 2/c* (#15)
a (Å)	9.06908
b (Å)	5.24654
c (Å)	13.21038
α	90.000
β	103.408
γ	90.000
Cr	8f (0.2768 0.4000 0.0792) Occupancy of Cr = 5.435 and Sc = 2.565 8f (0.6077 0.4033 0.0750) Occupancy of Cr = 5.712 and Sc = 2.288
Sc	8f (0.9547 0.40099 0.1090) Occupancy of Sc = 8.00
Al	8f (0.7393 0.1575 0.2496) 4e (0.00000 0.8956 0.25000)
C	8f (0.4401 0.2036 0.00000) 4d (0.25000 0.25000 0.50000)

Table S3. Elastic constants (in GPa) for nonmagnetic (NM), ferromagnetic (FM), and antiferromagnetic (AFM$[0001]^{X}_{4}$) $(Cr_{2/3}Sc_{1/3})_2AlC$.

	$(Cr_{2/3}Sc_{1/3})_2AlC$					
	NM		FM		AFM$[0001]^{X}_{4}$	
	Cmcm	*C*2/*c*	*Cmcm*	*C*2/*c*	*Cmcm*	*C*2/*c*
C_{11}	140	276	144	271	275	268
C_{22}	151	286	154	280	277	273
C_{33}	137	297	136	289	268	278
C_{44}	201	117	197	114	98	116
C_{55}	202	99	198	98	100	98
C_{66}	236	101	231	101	116	101
C_{12}	50	100	60	84	38	85
C_{13}	100	99	91	79	88	81
C_{23}	100	58	81	55	83	49
C_{15}		56		48		43
C_{25}		51		55		41
C_{35}		58		52		47
C_{46}		-1.18		-1.34		-1.53

Table S4. Elastic constants (in GPa) for nonmagnetic (NM), ferromagnetic (FM), and antiferromagnetic (AFM$[0001]_4^X$) $(Cr_{2/3}Y_{1/3})_2AlC$.

	$(Cr_{2/3}Y_{1/3})_2AlC$					
	NM		FM		AFM$[0001]_4^X$	
	Cmcm	*C*2/*c*	*Cmcm*	*C*2/*c*	*Cmcm*	*C*2/*c*
C_{11}	265	235	271	234	328	234
C_{22}	290	266	292	280	283	273
C_{33}	229	282	227	286	226	277
C_{44}	98	109	95	110	95	110
C_{55}	96	96	96	95	86	94
C_{66}	112	98	110	97	109	97
C_{12}	54	89	63	74	63	76
C_{13}	89	88	82	74	109	74
C_{23}	87	57	72	63	72	59
C_{15}		67		88		71
C_{25}		75		111		87
C_{35}		74		92		77
C_{46}		-1.09		-1.17		-1.84